Superfluid hydrodynamics in the inner crust of neutron stars

Noël Martin[*] and Michael Urban[†]

Institut de Physique Nucléaire, CNRS/IN2P3, Université Paris-Sud, and Université Paris-Saclay, F-91406 Orsay Cedex, France

The inner crust of neutron stars is supposed to be inhomogeneous and composed of dense structures (clusters) that are immersed in a dilute gas of unbound neutrons. Here we consider spherical clusters forming a body-centered cubic (BCC) crystal and cylindrical rods arranged in a hexagonal lattice. We study the relative motion of these dense structures and the neutron gas using superfluid hydrodynamics. Within this approach, which relies on the assumption that Cooper pairs are small compared to the crystalline structures, we find that the entrainment of neutrons by the clusters is very weak since neutrons of the gas can flow through the clusters. Consequently, we obtain a low effective mass of the clusters and a superfluid density that is even higher than the density of unbound neutrons. Consequences for the constraints from glitch observations are discussed.

I. INTRODUCTION

The inner crust of neutron stars is characterized by the presence of clusters in a more dilute gas of unbound neutrons. While the clusters, containing protons and neutrons, form probably a periodic lattice in order to minimize the Coulomb energy, the neutron gas is superfluid. The superfluid component of the crust can have potentially observable consequences for the hydrodynamical and thermodynamical properties of the crust [1]. It is therefore important to know the density of effectively free neutrons. This is a nontrivial problem because even the unbound neutrons might be "entrained" by the clusters because of their interactions.

This entrainment effect has already been extensively discussed in the literature [2], mostly in the framework of a band-structure theory for neutrons developed by Chamel and co-workers [3–5]. This theory predicts that a large fraction of the free neutrons are entrained. Consequently, the density of effectively free superfluid neutrons is strongly reduced. However, as discussed in Refs. [6,7], it is difficult to reconcile this reduction of the superfluid density with the observed glitch activity of the Vela pulsar.

The entrainment has also a strong effect on the heat transport properties of the crust, and consequently on the cooling of the star, through a modification of the speed of lattice and superfluid phonons [8,9]. These have been discussed in the framework of an effective theory for low-energy, long-wavelength excitations [10]. A long wavelength means in this context a wavelength that is large compared to the periodicity of the crystalline structures in the crust. This effective theory has a couple of parameters that have to be determined from more microscopic approaches. Among these parameters are the effective masses of the clusters, or, equivalently, the superfluid density.

However, under the assumption that pairing is sufficiently strong, superfluid hydrodynamics can also be applied on length scales that are smaller than the periodicity of the crystalline structures. This idea was used in [11–14] to estimate the

effective mass of an isolated cluster immersed in a neutron gas, and more recently also to describe collective modes in the so-called "lasagne" phases in the deepest layers of the inner crust [15,16]. In the present work, we apply this superfluid hydrodynamics approach also to the crystalline and "spaghetti" phases.

In Sec. II A, we briefly summarize the hydrodynamic model and the underlying assumptions. Then we apply it to the uniform motion of a crystalline lattice of clusters relative to the neutron gas (Sec. II B) and discuss how it can be related to the macroscopic entrainment (Sec. II C). In Sec. III, we explain how the hydrodynamic equations are solved. The properties of the specific geometries, namely the body-centered cubic (BCC) crystal of spherical clusters and the hexagonal lattice of cylindrical rods, are discussed in Sec. IV. Numerical results for microscopic and macroscopic quantities and consequences for the interpretation of glitches are presented in Sec. V. We conclude with a discussion in Sec. VI.

Except in Sec. V C and in the Appendix, we use units with $\hbar = c = 1$, where $\hbar$ is the reduced Planck constant and c the speed of light.

II. FORMALISM

A. Hydrodynamic model for the inner crust

Let us briefly recall the simple hydrodynamic model of Refs. [12–14,16]. We assume that the clusters have constant neutron and proton densities $n_{n,2}$ and $n_{p,2}$ and a sharp surface separating them from the neutron gas, whose density $n_{n,1}$ is also constant. The densities have to satisfy the conditions of phase equilibrium (equal chemical potentials and pressure in both phases), which is actually a very good approximation [17].

Furthermore, it is assumed that the neutrons are superfluid. Therefore, low-energy excitations correspond to coherent flow of Cooper pairs. If the superfluid order parameter (gap) is written as $\Delta = |\Delta|e^{i\varphi}$, the velocity field of the neutron pairs is related to the phase φ by $\mathbf{v}_n = \nabla\varphi/(2m)$, where m denotes the neutron mass.[1] In the limit of zero temperature, and if one

---

[*]noelmartin@ipno.in2p3.fr

[†]urban@ipno.in2p3.fr

---

[1]In contrast to Refs. [15,16] we neglect here the "microscopic" entrainment of neutrons by protons in the liquid phase [18], which
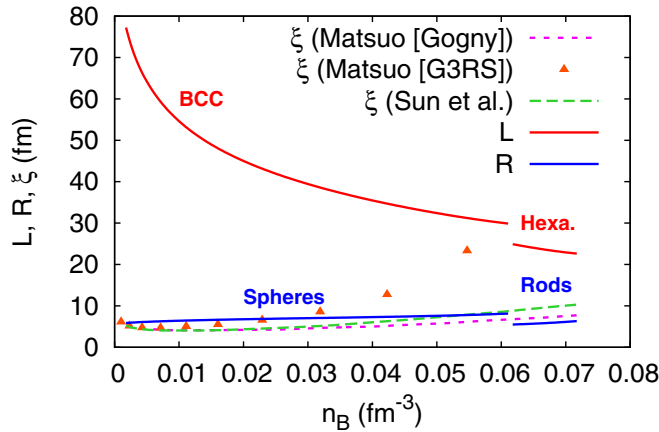
FIG. 1. Root-mean-square radius ξ of the Cooper pair in the neutron gas (dashed lines) compared with the cell size L of the crystalline lattice (red solid line) and the cluster radius R (blue solid line) as functions of the total baryon density n_B in the inner crust. The neutron gas density $n_{n,1}$ and the shown results for L and R were obtained from calculations detailed in Ref. [17]. The results for ξ as functions of $n_{n,1}$ were obtained respectively by Matsuo [24] and Sun *et al.* [25] using the Gogny force (purple short dashes), the G3RS force (orange triangles), and the Bonn potential (green long dashes) as pairing interactions.

excludes pair breaking, this leads to the equations of superfluid hydrodynamics as discussed in Refs. [19,20] in the context of ultracold atoms. Let us also mention that, again in the context of ultracold atoms, a calculation in quasiparticle random-phase approximation (QRPA) [21] showed that the collective modes can be described by hydrodynamics if $|\Delta|$ becomes much larger than the spacing of the discrete single-particle levels in the trap potential.

In uniform neutron matter, the QRPA shows that the hydrodynamic behavior of the oscillations of the phase φ (Goldstone or Bogoliubov-Anderson mode) is well fulfilled as long as the excitation energy stays well below the two-quasiparticle (pair breaking) threshold [22]. Furthermore, QRPA calculations of collective modes of a cluster in a spherical Wigner-Seitz (WS) cell predicted the appearance of "supergiant" resonances that could be interpreted as hydrodynamic Bogoliubov-Anderson modes in the volume of the cell [23].

In a nonuniform system, hydrodynamics is valid if the coherence length ξ of the Cooper pairs is small compared to the size of the inhomogeneities. In Fig. 1, we show different theoretical predictions of the Cooper pair size ξ in the neutron gas. While the results obtained with the Gogny force [24] are in good agreement with those obtained with the Bonn potential [25], the coherence length obtained with the G3RS force [24] is considerably larger, especially at higher densities $n_{n,1}$. Actually, the uncertainty in ξ is directly related to the fact that the density dependence of the gap Δ in neutron matter is not very well known. From now on we will assume that pairing

originates from the velocity dependence of the effective neutron-proton interaction. It should be included in future studies.

is strong, as with the Gogny or Bonn interactions. Note that the coherence length is also relevant for the spatial structure of vortices [26,27].

In Fig. 1, we also display the size L of the unit cell of the crystalline lattice and the radius R of the clusters obtained in Ref. [17]. Although the exact numbers for L and R depend on the model, their order of magnitude follows from the balance between surface and Coulomb energy and is therefore much better constrained than the coherence length. We see that, at low densities, the Cooper pair size ξ in the neutron gas is indeed much smaller than the size L of the unit cell of the crystalline lattice. At higher densities, where one expects the pasta phases, the comparison would be somewhat less favorable. However, the main problem is the small size of the clusters, whose radii R are as small as ξ even in the case of strong pairing.

The condition $\xi \ll R$ for the validity of hydrodynamics was already mentioned in Migdal's seminal work [28] in which he explained the nuclear moments of inertia in the framework of the theory of superfluidity. Since the coherence length ξ and the nuclear radius R are of the same order of magnitude, rotating nuclei exhibit a combination of irrotational and rotational flow. Nevertheless, the nuclear moments of inertia are slightly closer to the irrotational (hydrodynamic) than to the rigid-body limit (see Fig. 8.2 in Ref. [29]).

In analogy to this observation, we expect that probably our superfluid hydrodynamic model for the inner crust should give the right picture, although it might probably overestimate the superfluid flow inside (and close to) the clusters. We refer to Sec. VI for a further discussion of this problem and possible solutions.

B. Uniform flow of clusters through the gas

In the present paper, we concentrate on macroscopic (long wavelength) motion. In this case, the relative velocity between clusters and neutron gas varies only on length scales that are much larger than the periodicity of the lattice.

We limit ourselves to a stationary motion, i.e., we assume that the velocities and densities are time-independent in the rest frame of the clusters. Then, in the limit of small velocities, the size and shape of the clusters themselves as well as the densities in the clusters and in the gas do not change as compared to the static case. We define the cluster surface as the surface of the sphere (3D) or rod (2D) containing the protons. Hence, the velocity of the clusters is equal to the velocity of the protons, $\mathbf{u}_p$. The neutrons, however, can pass through the cluster surface, and their velocity field $\mathbf{v}_n(\mathbf{r})$ is not uniform, since the neutrons of the gas somehow have to flow around or through the clusters. To determine this motion is the main goal of the present work.

As mentioned in Sec. II A, the superfluidity of the neutron gas allows us to introduce a velocity potential $\phi = \varphi/(2m)$. Since the densities remain constant, we have $\boldsymbol{\nabla} \cdot \mathbf{v}_n = 0$, i.e.,

$$\triangle \phi = 0. \tag{1}$$

This equation is true in both phases, but it has to be complemented with suitable boundary conditions at the phase boundaries.

In Refs. [11,15], the phase boundary was treated as impermeable. However, this is not realistic, since neutrons inside and outside the cluster are indistinguishable and nothing prevents them from moving from the gas into the cluster or vice versa. The permeability of the phase boundary was included in the boundary conditions introduced by Magierski and Bulgac [12–14]. Analogous boundary conditions were given in Ref. [30] for a phase boundary in the context of ultracold atoms. They were also used in Ref. [16] to describe collective modes in the "pasta" phases of the neutron-star crust.

First, the phase of the order parameter is continuous across the phase boundary, i.e.,

$$\phi_1 = \phi_2, \tag{2}$$

where 1 and 2 refer to the limits of $\mathbf{r}$ approaching the interface from outside or inside the cluster, respectively. This boundary condition implies that the neutron velocity tangential to the interface is continuous, too.

Second, the neutron current crossing the interface conserves the particle number. Since the interface itself moves with velocity $\mathbf{u}_p$, this condition reads

$$n_{n,1}(\nabla\phi_1 - \mathbf{u}_p) \cdot \mathbf{S} = n_{n,2}(\nabla\phi_2 - \mathbf{u}_p) \cdot \mathbf{S}, \tag{3}$$

where $\mathbf{S}$ is the normal vector to the surface, pointing outwards. Note that in the limiting case of a vanishing gas density ($n_{n,1} = 0$), this equation implies that $\nabla\phi_2 = \mathbf{u}_p$, i.e., in this case the neutrons inside the cluster move together with the protons as is intuitively clear.

So far, the boundary conditions are the same as in Ref. [12–14], where the motion of a spherical nucleus in an infinite neutron gas was studied. In this case, Eqs. (1)–(3) can be solved analytically (see Sec. III A). However, except in the case of plates (1D), this is no longer true if one considers a periodic lattice of clusters.

To treat the periodicity, we introduce a primitive cell $\mathcal{C}$ spanned by the D primitive vectors $\mathbf{a}_i$ ($i = 1, \ldots, D$) of the Bravais lattice, where $D = 3$ in the case of a crystal, $D = 2$ in the case of rods (spaghetti phase), and $D = 1$ in the case of plates (lasagne phase). Depending on the lattice structure, the primitive cell contains one or two clusters (see Sec. IV). While the velocity field $\mathbf{v}_n(\mathbf{r})$ is periodic,

$$\mathbf{v}_n(\mathbf{r} + \mathbf{a}_i) = \mathbf{v}_n(\mathbf{r}), \tag{4}$$

the velocity potential itself can in general be the sum of a periodic and a linear function. The linear function can be written as $\mathbf{u}_n \cdot \mathbf{r}$, where $\mathbf{u}_n$ is the spatially averaged neutron velocity, which coincides with the velocity of the *superfluid* neutrons [9,31] or *conduction* neutrons [8]. Note that $\mathbf{u}_n$ is different from the average neutron velocity $\bar{\mathbf{v}}_n$, which is defined via the spatially averaged neutron current (see below). Without loss of generality, let us choose the frame of reference such that $\mathbf{u}_n = 0$. In this frame, also the velocity potential is periodic,

$$\phi(\mathbf{r} + \mathbf{a}_i) = \phi(\mathbf{r}). \tag{5}$$

From the function $\phi(\mathbf{r})$ in the primitive cell one can derive the macroscopic (coarse grained) neutron current $\bar{\mathbf{j}}_n$

by averaging over the volume of the cell, V_C:

$$\bar{\mathbf{j}}_n = \frac{1}{V_C} \int_{\mathcal{C}} dV \, n_n(\mathbf{r}) \nabla\phi(\mathbf{r}). \tag{6}$$

After integration by parts, Eq. (6) reduces to

$$\bar{\mathbf{j}}_n = \frac{1}{V_C}(n_{n,2} - n_{n,1}) \oint_{\Omega} d\mathbf{S} \, \phi(\mathbf{r}), \tag{7}$$

where Ω is the surface of the cluster(s) in the cell. The integral over the cell boundary vanishes because of the periodicity of ϕ.

Similarly, one can calculate the average kinetic energy density

$$\mathcal{E}_{\mathrm{kin},n} = \frac{m}{2V_C} \int_{\mathcal{C}} dV \, n_n(\mathbf{r})[\nabla\phi(\mathbf{r})]^2. \tag{8}$$

Using the Gauss theorem and Eq. (3), this expression can be simplified to [12]

$$\mathcal{E}_{\mathrm{kin},n} = \frac{m}{2V}(n_2 - n_1) \oint_{\Omega} d\mathbf{S} \cdot \mathbf{u}_p \phi(\mathbf{r}) = \frac{m}{2} \mathbf{u}_p \cdot \bar{\mathbf{j}}_n. \tag{9}$$

C. Entrainment

In Eq. (5) we assumed that $\mathbf{u}_n = 0$. The solution for ϕ in the general case $\mathbf{u}_n \neq 0$ is related to the periodic solution in the special case $\mathbf{u}_n = 0$ by

$$\phi(\mathbf{r}; \mathbf{u}_p, \mathbf{u}_n) = \mathbf{r} \cdot \mathbf{u}_n + \phi(\mathbf{r}; \mathbf{u}_p - \mathbf{u}_n, 0). \tag{10}$$

The average velocity of neutrons $\bar{\mathbf{v}}_n$ is defined via the average current $\bar{\mathbf{j}}_n$ as

$$\bar{\mathbf{v}}_n = \frac{\bar{\mathbf{j}}_n}{\bar{n}_n}, \tag{11}$$

where

$$\bar{n}_n = \frac{V_1}{V_C} n_{n,1} + \frac{V_2}{V_C} n_{n,2} \tag{12}$$

denotes the average neutron density with $V_{1,2}$ the volume outside and inside the cluster(s), respectively. The neutron current is now written as

$$\bar{\mathbf{j}}_n = \frac{1}{V_C} \int_{\mathcal{C}} dV \, n_n(r) \nabla\phi(\mathbf{r}; \mathbf{u}_p, \mathbf{u}_n)$$

$$= \bar{n}_n \mathbf{u}_n + \frac{1}{V_C} \int_{\mathcal{C}} dV \, n_n(r) \nabla\phi(\mathbf{r}; \mathbf{u}_p - \mathbf{u}_n, 0). \tag{13}$$

Since the last term in Eq. (13) is linear in $\mathbf{u}_p - \mathbf{u}_n$, we can write the current in the form

$$\bar{\mathbf{j}}_n = \bar{n}_n \mathbf{u}_n + \underline{\mathbf{n}}_n^b(\mathbf{u}_p - \mathbf{u}_n), \tag{14}$$

with a 3×3 matrix $\underline{\mathbf{n}}_n^b$. Factorizing Eq. (14) with respect to $\mathbf{u}_n$, one sees that $\underline{\mathbf{n}}_n^b$ can be interpreted as the density of bound neutrons, which are entrained by the clusters with velocity $\mathbf{u}_p$, while the superfluid neutrons moving with velocity $\mathbf{u}_n$ have an average density $\underline{\mathbf{n}}_n^s = \bar{n}_n \underline{\mathbf{I}}_3 - \underline{\mathbf{n}}_n^b$. Concerning bound and superfluid neutrons, we follow here the nomenclature of Ref. [31]. Hence, the final expression for the neutron current reads:

$$\bar{\mathbf{j}}_n = \underline{\mathbf{n}}_n^b \mathbf{u}_p + \underline{\mathbf{n}}_n^s \mathbf{u}_n. \tag{15}$$

The fact that $\underline{\mathbf{n}}_n^b$ and $\underline{\mathbf{n}}_n^s$ are matrices shows that the proportion of bound neutrons depends in general on the direction of the relative motion between neutrons and protons. This is intuitively clear, e.g., in the case of the 2D rod phase, where neutrons and protons can move independently of each other in the direction parallel to the rods, while this is not the case in the directions perpendicular to the rods. As will be shown in Sec. IV A, $\underline{\mathbf{n}}_n^b$ and $\underline{\mathbf{n}}_n^s$ are proportional to the unit matrix if the lattice has a cubic symmetry.

It is straightforward to generalize also Eq. (9) for the neutron kinetic energy to the general case $\mathbf{u}_n \neq 0$. First, note that in the case $\mathbf{u}_n = 0$, the current simplifies to $\bar{\mathbf{j}}_n = \underline{\mathbf{n}}_n^b \mathbf{u}_p$, and consequently Eq. (9) becomes $\mathcal{E}_{\text{kin},n} = (m/2)\mathbf{u}_p^\mathsf{T} \underline{\mathbf{n}}_n^b \mathbf{u}_p$. Starting from Eq. (10) and repeating the same steps for the general case $\mathbf{u}_n \neq 0$, one obtains:

$$\mathcal{E}_{\text{kin},n} = \frac{m}{2}\left(\mathbf{u}_n^\mathsf{T} \underline{\mathbf{n}}_n^s \mathbf{u}_n + \mathbf{u}_p^\mathsf{T} \underline{\mathbf{n}}_n^b \mathbf{u}_p\right), \qquad (16)$$

which agrees with the expression of Chamel and Carter [32] if one identifies n_n^b with the neutron *normal* density in their nomenclature.

In summary, the macroscopic entrainment coefficients of the crust are determined by the matrices $\underline{\mathbf{n}}_n^b$ and $\underline{\mathbf{n}}_n^s$ which we can obtain by solving numerically Eqs. (1)–(5) for the function $\phi(\mathbf{r}; \mathbf{u}_p, 0)$.

III. SOLUTION OF THE HYDRODYNAMIC EQUATIONS

A. Analytic solution in simple cases

In the case of a single cluster (spherical or cylindrical) moving with velocity $\mathbf{u}_p$ through in an infinite and uniform neutron gas, and in the case of a 1D lattice of parallel plates, analytical solutions for the velocity potential can be found.

The case of a spherical cluster of radius R was studied in Refs. [12–14]. If we place the origin of the coordinate system in the center of the cluster and suppose that the neutron gas is at rest at infinity ($\phi \rightarrow 0$ for $r \rightarrow \infty$), the solution for the velocity potential is

$$\phi(\mathbf{r}) = \begin{cases} \frac{1-\gamma}{1+2\gamma}\mathbf{r}\cdot\mathbf{u}_p & \text{for } r < R, \\ \frac{R^3}{r^3}\frac{1-\gamma}{1+2\gamma}\mathbf{r}\cdot\mathbf{u}_p & \text{for } r \geqslant R, \end{cases} \qquad (17)$$

where $\gamma = n_{n,1}/n_{n,2}$ is the ratio between the neutron densities in the gas and in the cluster. From this solution, one can compute the total momentum carried by neutrons in the cluster and in the gas. Identifying this momentum with $N_{\text{eff}} m \mathbf{u}_p$, one can define the number N_{eff} of neutrons effectively entrained by the protons of the cluster,

$$N_{\text{eff}} = N_{\text{r-cluster}}\frac{(1-\gamma)^2}{1+2\gamma}, \qquad (18)$$

with

$$N_{\text{r-cluster}} = \frac{4\pi}{3}R^3 n_{n,2} \qquad (19)$$

the number of neutrons that are located inside the cluster (in coordinate space, denoted r-cluster following Ref. [33]). It is interesting to note that $N_{\text{eff}} < N_{\text{r-cluster}}$, i.e., the main effect is not that the cluster entrains neutrons of the gas with it, but

rather that the flow of gas neutrons through the cluster surface reduces the speed of the neutrons inside the cluster.

The case of a cylindrical rod moving through an infinite and uniform neutron gas can be treated analogously. Here, the velocity potential is given by

$$\phi(\mathbf{r}) = \begin{cases} \frac{1-\gamma}{1+\gamma}\mathbf{r}_\perp\cdot\mathbf{u}_p & \text{for } r_\perp < R, \\ \frac{R^2}{r_\perp^2}\frac{1-\gamma}{1+\gamma}\mathbf{r}_\perp\cdot\mathbf{u}_p & \text{for } r_\perp \geqslant R, \end{cases} \qquad (20)$$

where $\mathbf{r}_\perp$ is the projection of $\mathbf{r}$ on the plane perpendicular to the symmetry axis of the rod. Since the rod is assumed to be infinite, one can only define N_{eff} and $N_{\text{r-cluster}}$ as numbers per unit length, e.g., $N_{\text{r-cluster}} = \pi R^2 n_{n,2}$. If the proton velocity $\mathbf{u}_p$ is parallel to the rod, the surface of the rod does not move and there is obviously no entrainment. However, for $\mathbf{u}_p$ perpendicular to the rod, the expression of effectively bound (entrained) neutrons reads as

$$N_{\text{eff}} = N_{\text{r-cluster}}\frac{(1-\gamma)^2}{1+\gamma}. \qquad (21)$$

One sees that the number of entrained neutrons is again lower than the number of neutrons geometrically located inside the rod.

Another case in which an analytic solution can be found is the phase of plates (1D). Let us consider alternating layers of phases 1 and 2 with widths L_1 and L_2, respectively. We take the layers parallel to the xy plane and choose the unit cell $0 < z < L = L_1 + L_2$ such that the region $0 < z < L_1$ corresponds to phase 1 and $L_1 < z < L$ to phase 2. Obviously the protons can entrain the neutrons only in z direction. In the rest frame of the superfluid neutrons, the solution for the velocity potential reads

$$\phi(\mathbf{r}) = \begin{cases} -\frac{1-\gamma}{L_1/L_2+\gamma}z u_{p,z} & \text{for } 0 \leqslant z \leqslant L_1, \\ \frac{1-\gamma}{1+\gamma L_2/L_1}(z-L)u_{p,z} & \text{for } L_1 \leqslant z \leqslant L. \end{cases} \qquad (22)$$

From this solution, one can readily obtain the density of bound neutrons (more precisely, the zz component of the matrix $\underline{\mathbf{n}}_n^b$; all other components vanish):

$$n_{n,zz}^b = \bar{n}_n\frac{(1-\gamma)^2 L_1 L_2}{(L_1+\gamma L_2)(L_2+\gamma L_1)}. \qquad (23)$$

In practice, $n_{n,zz}^b$ is much smaller than $\bar{n}_n$ ($n_{n,zz}^b/\bar{n}_n \lesssim 0.03$) because the plates are only found in the deepest layers of the neutron-star crust [17], where the density of the gas is quite large ($\gamma \gtrsim 0.7$).

B. Numerical solution

In 2D and 3D, the situation is more difficult if one considers instead of an isolated cluster a periodic lattice of clusters. Because of the different geometries of the clusters and of the lattice, the solution of the Laplace equation together with the boundary condition can only be obtained numerically in this case.

We start by discretizing the cell space with a regular mesh of N points per row. Note that if the unit cell is not cubic (as in the hexagonal 2D case, see Sec. IV), the rows are not orthogonal to one another. The cluster surface is approximated
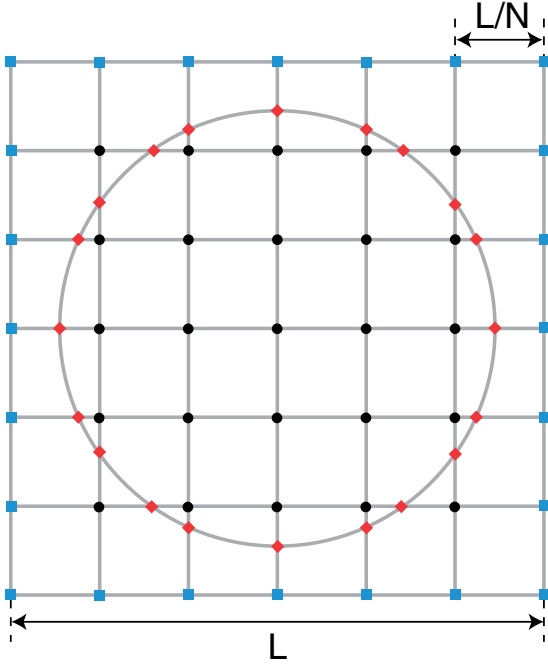
FIG. 2. Schematic illustration of the discretization of a simple cubic cell with a spherical cluster in its center.

by a set of N_S points given by the intersections of the mesh lines with the cluster surface. As an example, Fig. 2 illustrates the case of a spherical cluster in a simple cubic cell. Points belonging to the cell mesh are shown as black circles and blue squares, those belonging to the cluster surface as red diamonds. Because of periodicity, points lying on opposite edges of the cell, shown as blue squares, are equivalent to each other. In total, the number of independent points is $\mathcal{N} = N^D + N_S$. The numerical method for treating the periodicity is well described in Ref. [34].

Due to the space discretization, the differential equation (1)–(5) can be written as a linear system of equations. The solution is represented as a vector $\boldsymbol{\phi}$ of dimension $\mathcal{N}$ that contains the values of $\phi(\mathbf{x}_i)$, i.e., the solution of the differential equation in the points $\mathbf{x}_i$. In matrix form, the linear system of equations is written as

$$\underline{\mathbf{C}}\boldsymbol{\phi} = \mathbf{y}. \tag{24}$$

The elements of the $\mathcal{N} \times \mathcal{N}$ matrix $\underline{\mathbf{C}}$ are the coefficients of the $\phi(\mathbf{x}_i)$ in the discretized versions of the Laplace equation (1) for all but one mesh points and of the boundary condition (3) for the N_S surface points. To obtain a closed system, the Laplace equation in one of the mesh points, say, $\mathbf{x}_{i_0}$ (we choose it to be the center of the cell), is replaced by $\phi(\mathbf{x}_{i_0}) = 0$, since otherwise ϕ would only be determined up to an additive constant. The vector $\mathbf{y}$ of dimension $\mathcal{N}$ on the right-hand side of Eq. (24) contains the inhomogeneities arising from the boundary condition (3) due to the nonvanishing value of $\mathbf{u}_p$. Explicitly, its components read as

$$y_{i \notin \Omega} = 0, \tag{25}$$

$$y_{i \in \Omega} = (n_{n,1} - n_{n,2})\mathbf{S}_i \cdot \mathbf{u}_p, \tag{26}$$

where Ω denotes the surface points and $\mathbf{S}_i$ is the normal vector in the surface point i.

Let us also be more specific concerning the calculation of the matrix $\underline{\mathbf{C}}$. The rows $i \neq i_0$ of the matrix $\underline{\mathbf{C}}$ are defined as follows:

$$(\underline{\mathbf{C}}\boldsymbol{\phi})_{i \notin \Omega} = \triangle\phi(\mathbf{x}_i), \tag{27}$$

$$(\underline{\mathbf{C}}\boldsymbol{\phi})_{i \in \Omega} = \mathbf{S}_i \cdot [n_{n,1}\nabla\phi_1(\mathbf{x}_i) - n_{n,2}\nabla\phi_2(\mathbf{x}_i)], \tag{28}$$

while the i_0th row simply reads $C_{i_0 j} = \delta_{i_0 j}$. The Laplacian in Eq. (27) is expressed in terms of the second partial derivatives that are obtained by inverting the Taylor expansion

$$\phi(\mathbf{x}_j) = \phi(\mathbf{x}_i) + \sum_{\mu=1}^{D} \left.\frac{\partial\phi(\mathbf{x})}{\partial x_\mu}\right|_{\mathbf{x}_i} (x_{j,\mu} - x_{i,\mu})$$

$$+ \frac{1}{2}\sum_{\mu,\nu=1}^{D} \left.\frac{\partial^2\phi(\mathbf{x})}{\partial x_\mu \partial x_\nu}\right|_{\mathbf{x}_i} (x_{j,\mu} - x_{i,\mu})(x_{j,\nu} - x_{i,\nu}), \tag{29}$$

for $\{\mathbf{x}_j\}$ the nine (in 3D) or five (in 2D) closest and linearly independent points around $\mathbf{x}_i$. The indices μ and ν correspond to the spatial directions. In the special case of a 2D mesh with orthogonal axes (as in Fig. 2), one recovers in this way exactly the expressions given in Ref. [35] for the derivatives. For the one-sided normal derivatives on the surface in Eq. (28), two different sets of points $\{\mathbf{x}_j\}$ are used, containing only surface points and points outside the cluster for $\nabla\phi_1$, and only surface points and points inside the cluster for $\nabla\phi_2$.

In order to reduce the size of the matrix $\underline{\mathbf{C}}$ in memory, we use a sparse matrix storage (i.e., only nonzero matrix elements are stored). Unfortunately, the solution of Eq. (24) cannot be found with iterative methods (e.g., Gauss-Seidel) because the matrix is not positive definite. So a direct LU decomposition is needed, during which the size of the matrix blows up, which limits the maximum size of N.

IV. GEOMETRIES

A. Body-centered cubic lattice (3D)

In the less dense parts of the inner crust, one expects a Coulomb lattice of spherical clusters. The most favorable arrangement in space is probably a BCC lattice [36]. The primitive cell of this lattice, Fig. 3, has one cluster at its center and one eighth at each corner; i.e., it contains in total two clusters.

The BCC primitive cell presents symmetries simplifying the expressions for the average current and the kinetic energy. Assuming a velocity $\mathbf{u}_p$ in direction x and $\mathbf{u}_n = 0$, the average neutron current reads

$$\bar{\mathbf{j}}_n = \underline{\mathbf{n}}_n^b \mathbf{u}_p = \begin{pmatrix} n_{n,11}^b \\ n_{n,21}^b \\ n_{n,31}^b \end{pmatrix} u_p, \tag{30}$$

with $n_{n,ij}^b$ the elements of the matrix $\underline{\mathbf{n}}_n^b$ in the basis $\{\mathbf{e}_x, \mathbf{e}_y, \mathbf{e}_z\}$. Because of the symmetry $y \leftrightarrow -y$ and $z \leftrightarrow -z$, the current $\bar{\mathbf{j}}_n$ cannot have any component in y or z directions; i.e., the off-diagonal elements $n_{n,21}^b$ and $n_{n,31}^b$ must vanish. Repeating
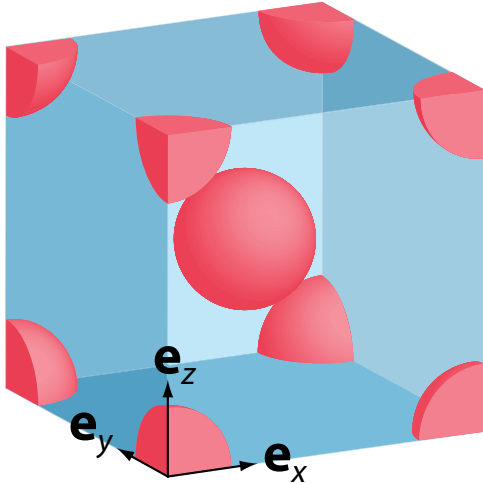
FIG. 3. Primitive cell of a BCC lattice of spherical clusters.

the same arguments for velocities $\mathbf{u}_p$ in y or z directions, one finds that all off-diagonal elements are zero.

Furthermore, the directions x, y, and z are equivalent in BCC symmetry. Thus all diagonal terms are equal, and the matrix simply reduces to a scalar matrix $\underline{\mathbf{n}}_n^b = n_n^b \underline{\mathbf{I}}_3$. So finally, in the BCC lattice, for $\mathbf{u}_n = 0$, $\bar{\mathbf{j}}_n$ and $\mathcal{E}_{\mathrm{kin},n}$ are simply given by

$$\bar{\mathbf{j}}_n = n_n^b \mathbf{u}_p \quad \text{and} \quad \mathcal{E}_{\mathrm{kin},n} = \frac{m}{2} n_n^b \mathbf{u}_p^2, \tag{31}$$

and there is no effect of anisotropy.

B. Hexagonal lattice (2D)

Deeper in the crust, clusters are supposed to be rods of bound nucleons [37]. In this case the most favored arrangement with respect to the Coulomb energy is a hexagonal lattice [36]. The primitive cell is a rhombus of side length L, height $\sqrt{3}L/2$, and an angle of $\pi/3$, as shown in Fig. 4. From the symmetry
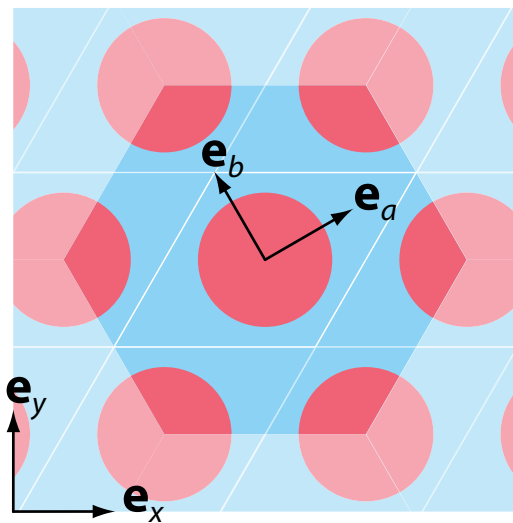

FIG. 4. Cut through a hexagonal lattice of cylindrical rods. The primitive cell is the parallelogram delimited by the white lines.

of the cell it is clear that the eigenvectors of $\underline{\mathbf{n}}_n^b$ are $\mathbf{e}_a$, $\mathbf{e}_b$, and $\mathbf{e}_z$ with

$$\begin{pmatrix} \mathbf{e}_a \\ \mathbf{e}_b \end{pmatrix} = \begin{pmatrix} \frac{\sqrt{3}}{2} & \frac{1}{2} \\ -\frac{1}{2} & \frac{\sqrt{3}}{2} \end{pmatrix} \begin{pmatrix} \mathbf{e}_x \\ \mathbf{e}_y \end{pmatrix}. \tag{32}$$

The vectors $\mathbf{e}_a$ and $\mathbf{e}_b$ are shown in Fig. 4. The three directions (a,b,z) are, however, not equivalent, thus in the basis $\{\mathbf{e}_a, \mathbf{e}_b, \mathbf{e}_z\}$ the diagonal elements (eigenvalues) of $\underline{\mathbf{n}}_n^b$ are all different: $n_{n,11}^b \neq n_{n,22}^b \neq n_{n,33}^b$. Let us note that the rods are invariant with respect to the z axis; i.e., all neutrons can move freely in that direction, consequently $n_{n,33}^b = 0$.

V. RESULTS

A. Microscopic flow

We solve Eqs. (1)–(3) for a fixed velocity $\mathbf{u}_p$ of the clusters. As input for the radius of the clusters, the densities inside and outside the clusters, and the cell size, we use results obtained in Ref. [17] within the extended Thomas-Fermi (ETF) method with a Skyrme energy-density functional (SLy4). Figure 5 shows streamlines (left panels) and velocity potential (right panels) in a BCC cell, in the case of $\mathbf{u}_p$ in x direction. The neutron-fluid streamlines are displayed as white arrows; they characterize the flow direction and are tangential to the velocity field vectors. The background color scheme indicates the speed, from dark purple in the slowest zones to red in the fastest ones. We chose two cuts through the cell parallel to the xy plane. The upper panels correspond to the plane through the center of the cell ($z = 0$), while the lower panels correspond to a plane between the clusters ($z = L/4$). In Fig. 5(a) the neutron velocity inside the cluster $\mathbf{v}_{n,2}$ is practically constant but lower than the velocity $\mathbf{u}_p$ of the surface. Here the ratio between the fluid and the surface velocity is $|\mathbf{v}_{n,2}|/|\mathbf{u}_p| = 0.284$, which can be compared with the analytic result (17) for the neutron velocity inside a cluster moving through an infinite neutron gas: $(1 - \gamma)/(1 + 2\gamma) = 0.315$.

Furthermore one sees that neutrons between the clusters move in the opposite direction. The velocity discontinuity at the cluster surface satisfies the boundary condition (3) of the conservation of the neutron current crossing the surface. When going away from the cluster surface, we observe that the speed decreases because the flux is spread over a larger area. Figures 5(c) and 5(d) show the plane between the clusters at $z = L/4$. One can observe on the edges of the cell the periodicity of the field. The five red areas correspond to the regions that are closest to the clusters.

Let us now discuss the case of the hexagonal lattice shown Fig. 6. Qualitatively, the behavior is similar to the one observed in the BCC lattice. However, in contrast to the BCC case, the hexagonal primitive cell is not isotropic. Thus we performed calculations with velocities $\mathbf{u}_p$ in the directions of the eigenvectors $\mathbf{e}_a$ and $\mathbf{e}_b$ (cf. Sec. IV B). One can clearly see a strong difference of the periodic behavior between Fig. 6(a) and Fig. 6(c), especially at the corners of the primitive cell. In Fig. 6(c), the streamlines continue straight to the next cell, while in Fig. 6(a) they deviate from their initial trend $\mathbf{e}_a$. Instead of exiting or entering through the corners of the cell, the flow passes through its sides and then through the neighboring

(a) Velocity field ($z = 0$)

(b) Velocity potential ($z = 0$)

(c) Velocity field ($z = L/4$)
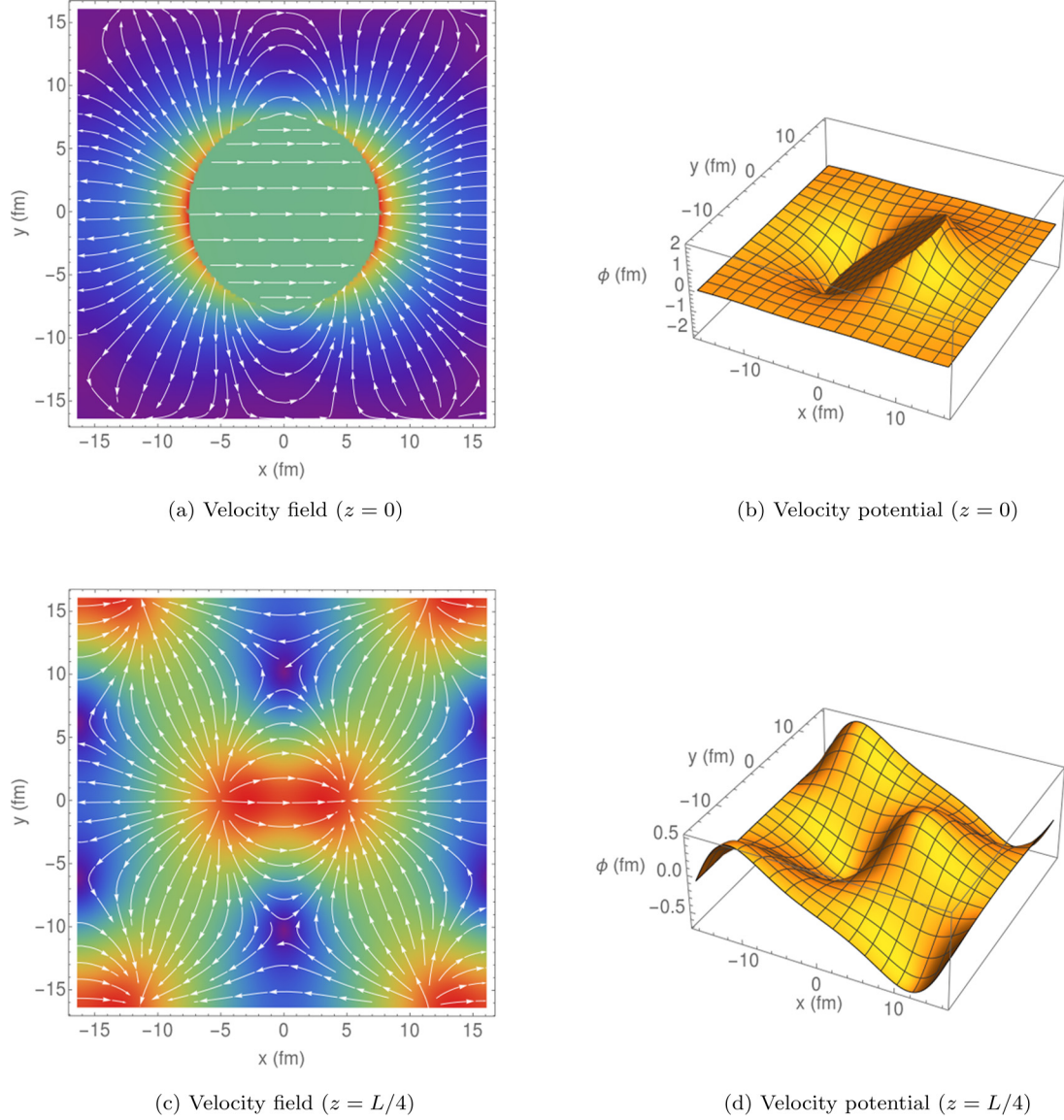

(d) Velocity potential ($z = L/4$)

FIG. 5. Streamlines and neutron speed (left) and velocity potentials (right) in a BCC cell of size $L = 32.8$ fm, with a cluster of radius $R = 7.54$ fm moving with velocity $\mathbf{u}_p = \mathbf{e}_x$. The neutron density inside the cluster is $n_{n,2} = 0.0973$ fm^{-3} and outside $n_{n,1} = 0.0412$ fm^{-3} (the cluster and cell properties were obtained from calculations described in Ref. [17] and correspond to a baryon density of $n_B = 0.0485$ fm^{-3}). In the left panels, the streamlines are shown as the white arrows, and the speed of the flow is indicated by the background color from dark purple (slowest) to red (fastest).

clusters situated in the directions of the translation vectors $\mathbf{a}_1$ and $\mathbf{a}_2$ of the Bravais lattice (parallel to the white lines in Fig. 4). Hence, the currents and the energies depend on the direction of $\mathbf{u}_p$. Nevertheless, the anisotropy effect on the ratio $|\mathbf{v}_{n,2}|/|\mathbf{u}_p|$ is very weak; numerically one finds 0.244 and 0.248 in the cases of $\mathbf{u}_p$ in direction $\mathbf{e}_a$ and $\mathbf{e}_b$, respectively. Similarly to the BCC case, this ratio is somewhat lower than the analytical result Eq. (20) for a single rod in an infinite gas, $|\mathbf{v}_{n,2}|/|\mathbf{u}_p| = 0.281$.

B. Cluster effective mass and superfluid density

With the help of Eq. (7), which is equivalent to averaging the microscopic current over the cell, one obtains the macroscopic quantities $\underline{\mathbf{n}}_n^s$ and $\underline{\mathbf{n}}_n^b$. In Sec. II C, they were interpreted as if

$\underline{\mathbf{n}}_n^s$ were the neutrons that move independently of the clusters while $\underline{\mathbf{n}}_n^b$ are the neutrons moving with the clusters. However, the preceding discussion of the microscopic flow shows that this is a simplified picture. In the BCC case, staying within this picture, we can define a cluster effective mass number

$$A_{\text{eff}} = N_{\text{eff}} + Z = \tfrac{1}{2} V_{\mathcal{C}} n_n^b + Z, \qquad (33)$$

where the factor $1/2$ accounts for the fact that there are two clusters per cell and Z is the number of protons in each cluster.

The cluster effective mass plays an important role for the calculation of the lattice phonons, as discussed, e.g., in [8,11,14]. It can be compared with the trivial result one obtains by counting all nucleons that are geometrically located inside the cluster, $A_{\text{r-cluster}} = N_{\text{r-cluster}} + Z$.

(a) Velocity field ($\mathbf{u}_p = \mathbf{e}_a$)

(b) Velocity potential ($\mathbf{u}_p = \mathbf{e}_a$)

(c) Velocity field ($\mathbf{u}_p = \mathbf{e}_b$)

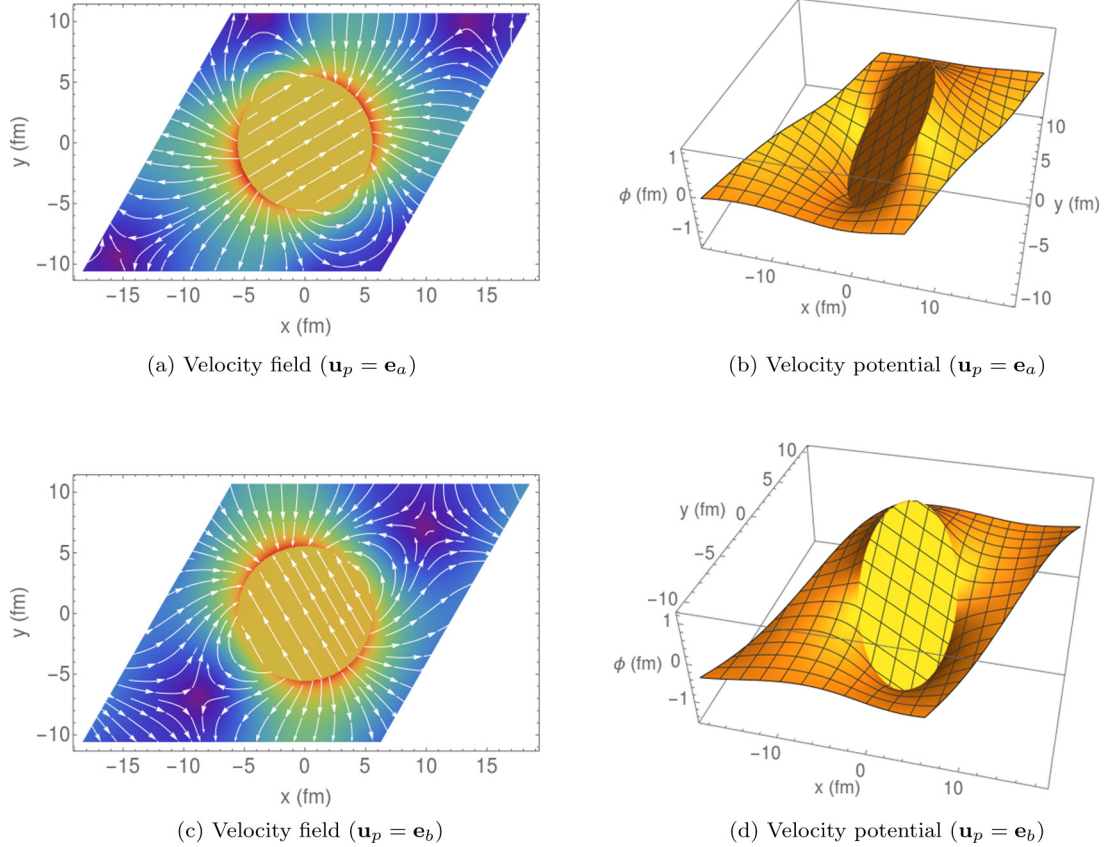(d) Velocity potential ($\mathbf{u}_p = \mathbf{e}_b$)

FIG. 6. Same as Fig. 5, but for a hexagonal cell of size $L = 24.7$ fm, containing a cylindrical rod of radius 5.53 fm moving with velocity $\mathbf{u}_p = \mathbf{e}_a$ (upper panels) or $\mathbf{e}_b$ (lower panels). The neutron density inside the rod is 0.0942 fm^{-3} and outside 0.0528 fm^{-3} (corresponding to a baryon density of $n_B = 0.0624$ fm^{-3}).

However, it might be more appropriate to define the cluster in energy space (e-cluster [33]). In this picture, neutrons are considered *free* or *confined* [32] (the word *bound* is also employed [3,33] but should not be confused with the effectively bound neutrons defined in Sec. II C) depending on their energy and independently of their position; i.e., free neutrons may also be located inside the cluster. In our approximation of constant densities in the two phases, the neutron Hartree-Fock mean field $U_n(\mathbf{r})$ is also constant in each phase and takes the values $U_{n,1}$ in the gas and $U_{n,2}$ in the cluster. Confined neutrons are characterized by a single-particle energy $\epsilon_n(\mathbf{k}) = k^2/(2m_n^*) + U_n$ that lies below the mean field in the gas, $\epsilon_n(\mathbf{k}) < U_{n,1}$, while the single-particle energy of free neutrons lies above, $\epsilon_n(\mathbf{k}) > U_{n,1}$; see Fig. 7. Hence, the
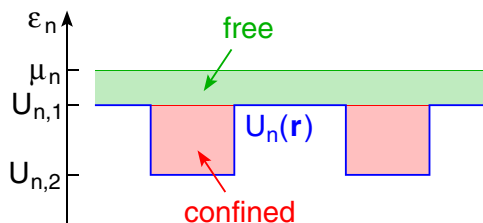
density of confined neutrons inside the cluster is in this picture given by

$$n_{n,2}^c = \frac{1}{3\pi^2}[2m_{n,2}^*(U_{n,1} - U_{n,2})]^{3/2}, \tag{34}$$

with $m_{n,i}^*$ the neutron effective mass calculated in phase i, and the remaining neutrons inside the cluster are free,[2]

$$n_{n,2}^f = n_{n,2} - n_{n,2}^c. \tag{35}$$

The effective neutron and mass numbers of the cluster (in energy space) are therefore

$$N_{\text{e-cluster}} = \frac{4\pi}{3} R^3 n_{n,2}^c \tag{36}$$

and $A_{\text{e-cluster}} = N_{\text{e-cluster}} + Z$. The mean fields $U_{n,i}$ and effective masses $m_{n,i}^*$ in Eq. (34) are calculated with the same Skyrme functional (SLy4) that was used in the ETF calculation of the cell properties [17].

In Fig. 8, we compare the effective neutron numbers of the clusters obtained within the different approaches as functions of the baryon density $n_B = \bar{n}_n + \bar{n}_p$. At low density, i.e., close to the outer crust, the density of the neutron gas is

FIG. 7. Schematic illustration of the definition of free and confined neutrons in energy space.

_____

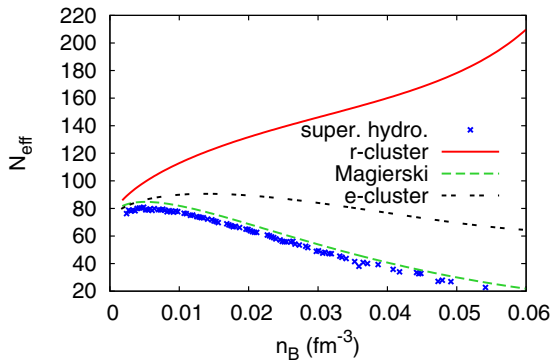[2]Here we do not distinguish between localized and unlocalized unbound neutrons [33].

FIG. 8. Effective neutron number of the clusters moving through the neutron gas as a function of the baryon density n_B. The results of our numerical calculations (blue crosses) are compared with the result of Eq. (18) by Magierski and Bulgac [12–14] for an isolated cluster in a uniform neutron gas (green dashed line), and with the neutron numbers (19) and (36) of the cluster defined in coordinate (red solid line) and energy (black double-dashed line) space, respectively.

FIG. 9. Fraction of superfluid neutrons, $n_n^s/\bar{n}_n$ as a function of the baryon density n_B. Results of the present superfluid hydrodynamics approach (red solid line) are compared with the result of band-structure calculations by Chamel [5] (black circles). We display also our results for the fraction of (energetically) free neutrons $n_n^f/\bar{n}_n$ (green dashes) and those obtained within the band-structure approach [5] (purple squares).

very low and all approaches converge towards the same result. However, at higher density, when the density of the neutron gas increases, the approaches start to differ considerably. More and more neutrons that are located inside the clusters (in coordinate space) are not bound in energy space. Therefore, the number of neutrons in the e-cluster (black double-dashed line) is considerably smaller than the number of neutrons in the r-cluster (red solid line).

However, the effective neutron number obtained within the present superfluid hydrodynamics approach (blue crosses) is even smaller: at the highest densities where one still expects the BCC lattice, one finds $N_{\text{e-cluster}}/N_{\text{r-cluster}} \approx 0.3$, while superfluid hydrodynamics predicts $N_{\text{eff}}/N_{\text{r-cluster}} \approx 0.1$. Quite surprisingly, even at the highest densities, where the unit cell is not very large compared to the cluster size, our numerical results stay quite close to the analytical ones, Eq. (18) one would obtain for an isolated cluster (green dashed line).

Concerning the (small) difference between the numerical results and those of Eq. (18), one might think that it comes from the restriction of the integration to a finite volume. Actually, one can easily derive a modified version of Eq. (18) where one integrates the neutron current $n_n \nabla \phi$ only up to the WS radius instead of infinity, but it turns out that the difference is negligible. The main reason for the difference between the numerical results and those of Eq. (18) is the change of the velocity potential ϕ itself due to the periodic boundary conditions.

Another quantity of interest is the superfluid density n_n^s. In Fig. 9 we show the superfluid fraction $n_n^s/\bar{n}_n$ as a function of the baryon density n_B. Unfortunately, we cannot perform numerical calculations at very low total densities (as they prevail near the outer crust), because the unit cells become too large. But it seems that at these low densities, the superfluid density obtained within our hydrodynamic approach (solid red line) agrees approximately with the density of free neutrons (green dashed line). At higher total neutron densities, the superfluid fraction is larger than the density of free neutrons
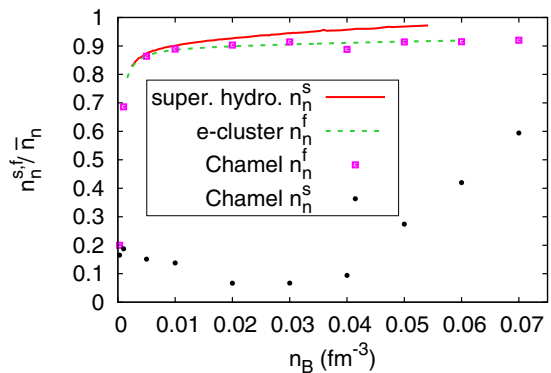
and it increases rapidly above 90%, exceeding 97% at the transition towards the 2D phase.

We compare these results with those obtained by Chamel [5] in the framework of the band theory for neutrons (black circles). This theory is analogous to the band theory in solid-state physics to describe electrons in the periodic Coulomb potential of a crystal [38]. In the inner crust of a neutron star, one has instead neutrons in the periodic mean field generated by the clusters. The superfluid density is in this approach obtained from an average of the Fermi velocity over the (highly nontrivial) Fermi surface [3,4,8]. While in our hydrodynamic approach the superfluid density is higher than the density of free neutrons, the band-structure calculation predicts a much lower superfluid density. Possible reasons for this discrepancy will be discussed in Sec. VI.

As a consistency check, we also compare our results for the fraction of free neutrons with those of the band-structure approach (purple squares), and for this quantity the agreement is excellent in spite of the crude approximations (sharp interface between the cluster and the gas, Thomas-Fermi approximation for the density of states) underlying Eq. (34).

So far we discussed the BCC lattice, where the densities of bound and superfluid neutrons are scalar quantities. The situation is different in the 2D hexagonal lattice of rods. In this case, if the velocity is parallel to the rods (z direction), the neutrons can move independently of the protons and the superfluid fraction is 100%. In the transverse plane, however, there is some entrainment. In Fig. 10, we show the densities of bound neutrons, n_n^b, for velocities in the directions of the eigenvectors $\mathbf{e}_a$ (red solid line) and $\mathbf{e}_b$ (green dashed line), as functions of the average neutron density in the density range where we expect to find the 2D phase, i.e., between ~ 0.06 and 0.07 fm^{-3} [17]. It can be seen that the anisotropy in the transverse plane, i.e., the difference between the directions a and b, is very small.
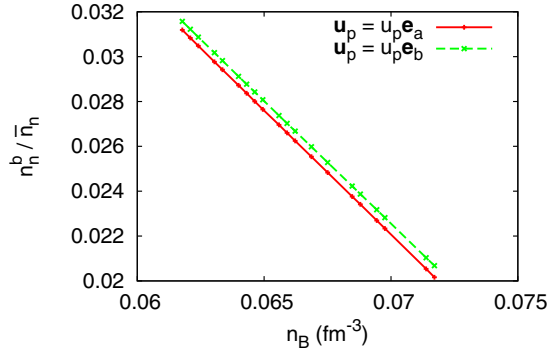
FIG. 10. Effective densities of bound neutrons in the 2D (spaghetti) phase for velocities in the directions of the two eigenvectors $\mathbf{e}_a$ and $\mathbf{e}_b$ as functions of total baryonic density.

C. Application to glitches

Glitches correspond to a sudden transfer of angular momentum from the superfluid to the normal parts of the star [39]. In the preceding sections, we discussed the densities of bound and superfluid neutrons in the inner crust. These quantities play a crucial role in the understanding of glitches in the neutron star [7,32]. In particular, as pointed out in Refs. [6,7], the observed glitches of the Vela pulsar can hardly be understood with the low superfluid fraction obtained in band structure theory. Since our results for the superfluid fraction are very different from those of band structure theory, let us discuss how this changes the conclusions from the glitch data. In this subsection, we follow to a large extent the arguments given in Refs. [7,32].

Let us assume that the superfluid and the normal parts of the star rotate at slightly different but spatially constant frequencies Ω_s and Ω_b, i.e., the velocity fields are given by $\mathbf{u}_p = \mathbf{\Omega}_b \times \mathbf{r}$ and $\mathbf{u}_n = \mathbf{\Omega}_s \times \mathbf{r}$.

Note that $\mathbf{u}_n$ has to be understood as the average velocity field on length scales that are large compared to the distance between the quantized vortices [40]. If we consider, e.g., a frequency of $\Omega_s = 100$ s^{-1}, the number of vortices per area is [41] $2m\Omega_s/(\pi\hbar) \approx 10^9$ m^{-2}; i.e., the vortices are separated by $\sim 30\,\mu$m. Since this distance is many orders of magnitude larger than the crystalline structures in the inner crust, one may use the results for n_n^s and n_n^b calculated for a uniform velocity field.

The total angular momentum of the star can now be decomposed into two contributions,

$$J = J_s + J_b = I_s\Omega_s + I_b\Omega_b, \tag{37}$$

where I_s and I_b are the moments of inertia of the superfluid and normal-fluid components, respectively:[3]

$$I_s = \int mn_n^s r_\perp^2 d^3r, \quad I_b = \int m(n_n^b + n_p)r_\perp^2 d^3r, \tag{38}$$

with $r_\perp = r\sin\theta$ the radial distance from the rotation axis.

---

[3]Note that, unlike in Ref. [32], there are no nondiagonal contributions to the angular momentum (contributions of Ω_s to J_b and vice versa) because we are working in the chemical basis of superfluid and bound neutrons, cf. Eq. (16).

As argued in Refs. [32,42], the entire core is probably rotating together with the nonsuperfluid part. Therefore, the superfluid contribution comes only from the superfluid neutrons in the inner crust, and the neutrons in the core are counted in n_n^b, although they are of course not bound to clusters.

Between two glitches, the observable frequency Ω_b is slowly decreasing because the emission of radiation leads to some loss of angular momentum of the normal component. Let us denote by $\Delta\Omega_b < 0$ the frequency change during the interglitch time. The superfluid component, however, is supposed to slow down much less than the normal component, e.g., because the vortices are pinned. Hence, the superfluid component can serve as a reservoir of angular momentum for the next glitch [42]. A glitch is interpreted as a sudden transfer of angular momentum from the superfluid to the normal fluid component. However, during the short duration of the glitch, the total angular momentum is conserved. Therefore, the differences of the frequencies before and after the glitch, denoted by $\delta\Omega_s$ and $\delta\Omega_b$, satisfy

$$I_s\delta\Omega_s + I_b\delta\Omega_b = 0. \tag{39}$$

Since $\Omega_s - \Omega_b$ cannot become too large, Ω_s must in average (after many glitches) decrease by the same amount as Ω_b, i.e.,

$$\langle\delta\Omega_s\rangle \geqslant \langle\Delta\Omega_b\rangle + \langle\delta\Omega_b\rangle, \tag{40}$$

where the equality corresponds to the limiting case that the superfluid does not slow down at all between two glitches ($\Delta\Omega_s = 0$). Combining Eq. (39) and (40), one arrives at the simple relation

$$\frac{I_s}{I} \geqslant -\frac{\langle\delta\Omega_b\rangle}{\langle\Delta\Omega_b\rangle} \equiv \mathcal{G}, \tag{41}$$

with $I = I_s + I_b$ the total moment of inertia of the neutron star, and $\mathcal{G}$ the *coupling parameter*, which is closely related to the *pulsar activity parameter* [42].

Following Ref. [7], one can make some additional approximations in order to obtain a quick estimate for the ratio I_s/I. First, we write $I_s/I = (I_{\rm crust}/I)(I_s/I_{\rm crust})$, where $I_{\rm crust}$ is the moment of inertia of the crust. For the crustal fraction of the moment of inertia, $I_{\rm crust}/I$, Lattimer and Prakash [43] gave an approximate expression that depends only on the pressure $P_{\rm core}$ and density $n_{\rm core}$ at the crust-core transition and on the total radius R and mass M of the star, but does not require detailed knowledge of the high-density equation of state (EOS) in the core. Moreover, making use of the thin crust approximation [44], one can derive the following simple expression for the superfluid contribution of the crustal moment of inertia [7]:

$$\frac{I_s}{I_{\rm crust}} = \frac{1}{P_{\rm core}} \int_{P_{\rm drip}}^{P_{\rm core}} \frac{n_n^s}{n_B} dP, \tag{42}$$

where $P_{\rm drip}$ is the pressure at the transition between the outer and the inner crust. Here, we use the EOS of the ETF model of the inner crust [17]. With our results for the superfluid density, we obtain $I_s/I_{\rm crust} \approx 0.94$. For the pasta phases with anisotropy (rods, plates), we assume that the orientation is random so that one can average the superfluid density over the three directions.
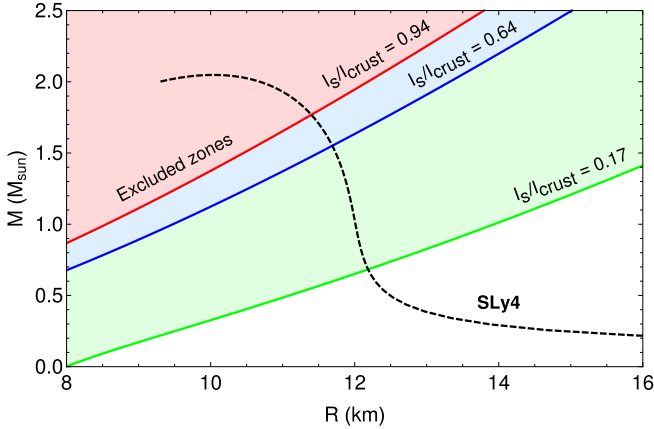
FIG. 11. Constraints on mass and radius of the Vela pulsar from its observed glitch activity for different superfluid fractions in the crust: hydrodynamic result $I_s/I_{crust} = 0.94$ (red), result from band-structure theory [7] $I_s/I_{crust} = 0.17$ (green), and an intermediate situation $I_s/I_{crust} = 0.64$ (blue) corresponding to hydrodynamics in the gas but no superfluidity in the clusters (see Sec. VI). We also show as an example the mass-radius relation obtained with the SLy4 interaction (dashed line). Note that other equations of state would lead to different mass-radius relations in a band around the shown one (see, e.g., Ref. [45] for an attempt to use observational data to constrain the width of this band).

For the Vela pulsar, one has $\mathcal{G} \approx 1.6\%$ [7]. With the approximations mentioned above and using our result $I_s/I_{crust} \approx 0.94$, this allows one to identify an excluded zone in the mass-radius diagram, shown in Fig. 11 in red. Details on the boundary of the excluded zone are given in the Appendix. No assumption has been made so far concerning the EOS in the core. To give a specific example, we show in Fig. 11 also the mass-radius relation obtained by solving the Tolman-Oppenheimer-Volkov (TOV) equations [46,47] with the EOS given by the SLy4 interaction in the whole star (for the outer crust, we use the results of Ref. [48]).[4] One sees that, with this EOS, Vela could have a mass of up to $1.7 M_{sun}$.

The strong entrainment predicted by band-structure theory results in a much smaller ratio $I_s/I_{crust} = 0.17$ [7]. As one can see from the corresponding excluded zone in the mass-radius diagram (zone above the green line in Fig. 11), this small superfluid fraction can only be conciliated with the observed glitch activity if either Vela is a very unusual neutron star with $M < 0.7 M_{sun}$ [7], or also the core has a superfluid component that can serve as a reservoir of angular momentum [6,7]. Another solution to this puzzle was suggested in Ref. [49], where it was pointed out that uncertainties in the EOS do not exclude the possibility that the crust could be much thicker than usually assumed.

However, in Fig. 11 we see that, with the much larger superfluid density predicted by our approach, the observed glitch activity is compatible with the assumption that Vela is a

---

[4]The calculation of the outer crust in Ref. [48] and our ETF model for the inner crust [17] are based on the SLy4 interaction.

perfectly normal neutron star, without any need for a superfluid core or an unusually thick crust.

VI. DISCUSSION

In this paper, we used a superfluid hydrodynamics approach to determine how the gas neutrons flow on a microscopic scale around and through the clusters when the crystal lattice of the clusters is uniformly and slowly moved through the gas. This allowed us to compute the densities of superfluid and bound (entrained) neutrons, n_n^s and n_n^b, and the effective mass of the clusters. Surprisingly, it turned out that n_n^s is larger than the density of free neutrons, n_n^f. As a consequence, the cluster effective mass number A_{eff} is not only smaller than the number of nucleons that are spatially located inside the cluster, but even smaller than the number of energetically bound nucleons.

Our results are in line with those obtained in Refs. [12–14] using the same hydrodynamic approach but for the case of an isolated cluster in an infinite neutron gas. However, in other studies, the opposite effect was found, namely that the effective mass of the clusters is increased by the presence of the gas.

For instance, in Ref. [11], a hydrodynamic approach was used, too, but with different boundary conditions at the interface between the cluster and the gas. In that work, the gas was assumed to flow around the cluster, increasing the total kinetic energy, while in our approach and that of Refs. [12–14] the permeability of the phase boundary allows the neutrons to flow through the cluster, reducing the neutron velocity inside the cluster and the total kinetic energy.

Studies of entrainment in the framework of band-structure theory [3,5] also predict a strong reduction of n_n^s as compared to n_n^f, and therefore a strong increase of A_{eff}. This approach was developed in analogy to band structure theory for electrons in condensed-matter physics. However, the situation of neutrons in the inner crust differs in some respects from the one of electrons in superconducting metals. In superconductors, the distance between the energy bands, of the order of a few eV, is much larger than the pairing gap Δ which is typically of the order of a few Kelvin (10^{-4} eV). This is why the pairing affects only electrons of the conduction band. The spatial extension of a Cooper pair of electrons is much larger than the unit cell of the crystal. In contrast, the neutron energy bands in the neutron-star crust lie very close to one another (cf. Figs. 2–4 in Ref. [5]): for a given quasimomentum $\mathbf{k}$, there can be many bands α whose energies $\epsilon_{\alpha \mathbf{k}}$ are separated by less than 1 MeV, which is the typical scale for the pairing gap Δ. This goes along with a coherence length ξ that is smaller than the unit cell.

For hydrodynamics to be quantitatively accurate, one would need a coherence length ξ that is also much smaller than the clusters. Since this condition is not satisfied, the true answer lies probably somewhere between the two models, i.e., the entrainment is maybe stronger than the one predicted by hydrodynamics, but weaker than the one predicted by band structure theory.

Coming back to the analogy with rotating nuclei which exhibit a mixture of rotational and irrotational flow as mentioned in Sec. II A, one might think about describing the
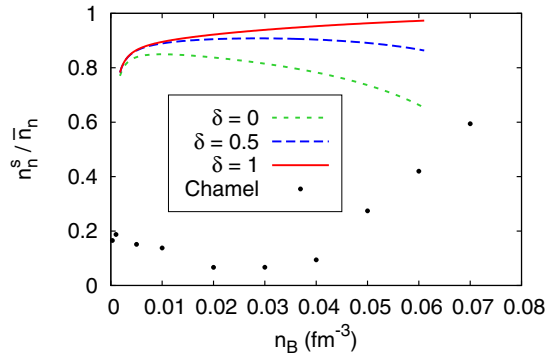
FIG. 12. Superfluid fraction $n_n^s/\bar{n}_n$ as a function of the baryon density n_B, obtained under the assumption that a fraction $\delta = 0$ (green short dashes), 0.5 (blue long dashes), or 1 (red solid line) of the neutrons in the clusters are superfluid. For comparison, the black circles are the result of the band-structure calculations by Chamel [5].

neutrons in the clusters as a mixture of superfluid neutrons, whose motion is governed by the phase φ of the gap, and normal-fluid neutrons, which move together with the protons. Recently it was suggested in the supplemental material of Ref. [50] to modify the hydrodynamic model of Refs. [12–14] in this sense by reinterpreting the densities $n_{n,1}$ and $n_{n,2}$ as effective superfluid densities. For instance, if we assume that all neutrons in the gas but only a fraction δ of the neutrons in the cluster participate in the superfluid motion, Eq. (18) for the effective mass of a single spherical cluster becomes

$$N_{\text{eff}} = N_{\text{r-cluster}}\left(1 - \delta + \frac{(\delta - \gamma)^2}{\delta + 2\gamma}\right). \quad (43)$$

Analogously, it is straightforward to generalize also Eqs. (21) and (23) to the case $\delta < 1$. In the extreme case $\delta = 0$ (no superfluidity inside the clusters, i.e., all neutrons in the cluster move together with the protons), one retrieves the picture of the gas flowing around the cluster as in Ref. [11], resulting in $N_{\text{eff}} = N_{\text{r-cluster}}(1 + \gamma/2)$. However, this extreme case does not seem to be realistic, since, e.g., in rotating nuclei at least one half of the nucleons follow the superfluid motion as one can conclude from the moments of inertia. Furthermore, we note that the present situation of a uniform flow of neutrons through the cluster is more favorable for hydrodynamics than the rotation of nuclei: while in a deformed nucleus rotating around the z axis the phase φ is proportional to xy [28], our phase is (inside the clusters) only linear in the coordinates. Therefore, δ should probably be larger than one half.

In analogy to the result of Sec. V B that N_{eff} in the periodic lattice follows closely the analytic formula (18), we can also compute the superfluid density $n_n^s = \bar{n}_n - 2N_{\text{eff}}/V_C$ with N_{eff} from Eq. (43). The resulting superfluid fractions for three values of δ are shown in Fig. 12. The case $\delta = 1$ corresponds to the one shown already in Fig. 9, but also for $\delta = 0.5$ and even in the extreme case $\delta = 0$ we obtain a superfluid density that is considerably larger than the one of Ref. [5].

Using the superfluid fraction obtained for $\delta = 0$ in Eq. (42), we find that the superfluid contribution to the moment of inertia of the crust would still be $I_s/I_{\text{crust}} \approx 0.64$. The corresponding

excluded region in the mass-radius diagram is the region above the blue line in Fig. 11 and, although it extends to lower masses than the result for $\delta = 1$ ($I_s/I_{\text{crust}} \approx 0.94$), it is still compatible with a mass of up to $\sim 1.5 M_{\text{sun}}$.

In any case, superfluid hydrodynamics remains a strongly simplified model, not only because of the assumption that the neutron motion is completely determined by the phase φ, but also because of the sharp surface of the clusters. To obtain more reliable results, one should ideally perform a QRPA calculation on top of a Hartree-Fock-Bogoliubov (HFB) ground state imposing the Bloch boundary conditions [38] on the single-particle wave functions as in band structure theory. However, at present this objective seems to be out of reach. Using a much simpler QRPA calculation in a spherical Wigner-Seitz (WS) cell, as in Ref. [23], could help to resolve at least the issues of the effective superfluid density in the cluster and the most realistic boundary conditions to be used in hydrodynamic calculations. Instead of the QRPA, one might also use the time-dependent superfluid local-density approximation (TDSLDA) [50,51]. Furthermore, as pointed out in Ref. [9], one should probably also consider zero-point oscillations of the clusters that would reduce the band-structure effects.

APPENDIX: BOUNDARY OF THE EXCLUDED ZONE IN THE MASS-RADIUS DIAGRAM

According to Eq. (41), the boundary between the allowed and the excluded zone in Fig. 11 corresponds to $I_s/I = \mathcal{G}$. As mentioned in Sec. V C, we follow Ref. [7] and decompose the ratio I_s/I as $(I_s/I_{\text{crust}})(I_{\text{crust}}/I)$. The factor (I_s/I_{crust}) is given by Eq. (42). For (I_{crust}/I), an analytic expression is given in Eq. (47) of Ref. [43], which can be written in a compact way as

$$\frac{I_{\text{crust}}}{I} = a_0(R)\frac{1 - 1.67\beta - 0.6\beta^2}{2a_1 + 10a_1\beta + (1 - 28a_1)\beta^2}. \quad (A1)$$

In this equation,

$$\beta = \frac{GM}{Rc^2} \quad (A2)$$

denotes the compactness of the star, with G the gravitational constant, M the mass of the star, and R its radius. The dimensionless coefficients a_i that appear in Eq. (A1) are given by

$$a_0(R) = \frac{28\pi G P_{\text{core}} R^2}{3c^4}, \quad a_1 = \frac{P_{\text{core}}}{n_{\text{core}} m c^2}, \quad (A3)$$

with P_{core} and n_{core} the pressure and the density at the crust-core transition, respectively, and m the neutron mass. Note that the expression (A1) for I_{crust}/I contains R and M as

independent variables because no assumption about the EOS in the core of the star is made, while it depends on the EOS in the crust through P_{core} and n_{core}. We use the values corresponding to our ETF model for the inner crust [17] based on the SLy4 interaction: $P_{core} = 0.38$ MeV fm^{-3} and $n_{core} = 0.081$ fm^{-3}.

For a given radius R, the compactness β and hence the mass M corresponding to the boundary of the excluded zone shown in Fig. 11 is now obtained as the solution of the quadratic equation

$$[0.6 + (1 - 28a_1)b(R)]\beta^2 + [1.67 + 10a_1b(R)]\beta$$
$$+ [1 + 2a_1b(R)] = 0, \tag{A4}$$

where $b(R)$ is defined as

$$b(R) = \frac{\mathcal{G}}{a_0(R)}\left(\frac{I_s}{I_{crust}}\right)^{-1}. \tag{A5}$$

[1] D. Page and S. Reddy, *Neutron Star Crust* (Nova Science, Hauppauge, NY, 2012), Chap. 14.

[2] R. Prix, G. L. Comer, and N. Andersson, Astron. Astrophys. **381**, 178 (2002).

[3] B. Carter, N. Chamel, and P. Haensel, Nucl. Phys. A **748**, 675 (2005).

[4] N. Chamel, Nucl. Phys. A **773**, 263 (2006).

[5] N. Chamel, Phys. Rev. C. **85**, 035801 (2012).

[6] N. Andersson, K. Glampedakis, W. C. G. Ho, and C. M. Espinoza, Phys. Rev. Lett. **109**, 241103 (2012).

[7] N. Chamel, Phys. Rev. Lett. **110**, 011101 (2013).

[8] N. Chamel, D. Page, and S. Reddy, Phys. Rev. C **87**, 035803 (2013).

[9] D. Kobyakov and C. J. Pethick, Phys. Rev. C **87**, 055803 (2013).

[10] V. Cirigliano, S. Reddy, and R. Sharma, Phys. Rev. C **84**, 045809 (2011).

[11] A. Sedrakian, Astrophys. Space Sci. **236**, 267 (1996).

[12] P. Magierski and A. Bulgac, Acta Phys. Pol. B **35**, 1203 (2004).

[13] P. Magierski and A. Bulgac, Nucl. Phys. A **738**, 143 (2004).

[14] P. Magierski, Int. J. Mod. Phys. E **13**, 371 (2004).

[15] L. Di Gallo, M. Oertel, and M. Urban, Phys. Rev. C **84**, 045801 (2011).

[16] M. Urban and M. Oertel, Int. J. Mod. Phys. E **24**, 1541006 (2015).

[17] N. Martin and M. Urban, Phys. Rev. C. **92**, 015803 (2015).

[18] M. Borumand, R. Joynt, and W. Kluźniak, Phys. Rev. C **54**, 2745 (1996).

[19] M. Urban and P. Schuck, Phys. Rev. A **73**, 013621 (2006).

[20] G. Tonini, F. Werner, and Y. Castin, Eur. Phys. J. D. **39**, 283 (2006).

[21] M. Grasso, E. Khan, and M. Urban, Phys. Rev. A **72**, 043617 (2005).

[22] N. Martin and M. Urban, Phys. Rev. C **90**, 065805 (2014).

[23] E. Khan, N. Sandulescu, and N. Van Giai, Phys. Rev. C **71**, 042801 (2005).

[24] M. Matsuo, Phys. Rev. C **73**, 044309 (2006).

[25] B. Y. S. Sun, H. Toki, and J. Meng, Phys. Lett. B **683**, 134 (2010).

[26] Ø. Elgarøy and F. V. De Blasio, Astron. Astrophys. **370**, 939 (2001).

[27] Y. Yu and A. Bulgac, Phys. Rev. Lett. **90**, 161101 (2003).

[28] A. B. Migdal, Nucl. Phys. **13**, 655 (1959).

[29] D. J. Rowe, *Nuclear Collective Motion. Models and Theory* (Methuen, London, 1970).

[30] A. Lazarides and B. Van Schaeybroeck, Phys. Rev. A **77**, 041602 (2008).

[31] C. J. Pethick, N. Chamel, and S. Reddy, Prog. Theor. Phys. Suppl. **186**, 9 (2010).

[32] N. Chamel and B. Carter, Mon. Not. R. Astron. Soc. **368**, 796 (2006).

[33] P. Papakonstantinou, J. Margueron, F. Gulminelli, and A. R. Raduta, Phys. Rev. C **88**, 045805 (2013).

[34] D. Evans and S. Okolie, J. Comput. Appl. Math. **8**, 237 (1982).

[35] D. Greenspan, J. Franklin Inst. **277**, 11 (1964).

[36] K. Oyamatsu, M.-a. Hashimoto, and M. Yamada, Prog. Theor. Phys. **72**, 373 (1984).

[37] D. G. Ravenhall, C. J. Pethick, and J. R. Wilson, Phys. Rev. Lett. **50**, 2066 (1983).

[38] N. Ashcroft and N. Mermin, *Solid State Physics* (Saunders College, Fort Worth, 1976).

[39] S. L. Shapiro and S. A. Teukolsky, *Black Holes, White Dwarfs and Neutron Stars: The Physics of Compact Objects* (Wiley-VCH, Weinheim, 2004).

[40] E. M. Lifshitz and L. P. Pitaevskii, *Statistical Physics, Part 2: Theory of the Condensed State*, Landau Lifshitz Course of Theoretical Physics No. 9 (Pergamon, Oxford, 1980).

[41] D. Pines and M. A. Alpar, Nature (London) **316**, 27 (1985).

[42] B. Link, R. I. Epstein, and J. M. Lattimer, Phys. Rev. Lett. **83**, 3362 (1999).

[43] J. M. Lattimer and M. Prakash, Phys. Rep. **333**, 121 (2000).

[44] C. P. Lorenz, D. G. Ravenhall, and C. J. Pethick, Phys. Rev. Lett. **70**, 379 (1993).

[45] A. W. Steiner, J. M. Lattimer, and E. F. Brown, Astrophys. J. Lett. **765**, L5 (2013).

[46] R. C. Tolman, Phys. Rev. **55**, 364 (1939).

[47] J. R. Oppenheimer and G. M. Volkoff, Phys. Rev. **55**, 374 (1939).

[48] F. Douchin and P. Haensel, Phys. Lett. B **485**, 107 (2000).

[49] J. Piekarewicz, F. J. Fattoyev, and C. J. Horowitz, Phys. Rev. C **90**, 015803 (2014).

[50] G. Wlazłowski, K. Sekizawa, P. Magierski, A. Bulgac, and M. McNeil Forbes, arXiv:1606.04847 [Phys. Rev. Lett. (to be published)].

[51] A. Bulgac, Annu. Rev. Nucl. Part. Sci. **63**, 97 (2013).